Journal of Materials Chemistry A

Cite this: DOI: 10.1039/c9ta00056a

Understanding the electrochemical potential and diffusivity of MnO/C nanocomposites at various charge/discharge states†

Chaofeng Liu,[a] Haoyu Fu,[b] Yanyan Pei,[a] Jiandong Wu,[c] Vivek Pisharodi,[a] Yang Hu,[a] Guohua Gao,[d] Robert J. Yang,[a] Jihui Yang *[a] and Guozhong Cao *[a]

Li-ion diffusion and lithiation kinetics in MnO/C nanocomposites were systematically investigated by monitoring the change in the charge transfer resistance and the ion diffusion coefficient, and the kinetically predominant process at various charge/discharge states. Crystal field analysis and density functional theory (DFT) calculations were introduced to reveal the relationship between the electronic structure of the phase compositions, the displayed electrochemical potential and its profile. The split 3d orbitals in the Mn ion determine the ordering of the electron migration and energy difference, leading to the different potential profiles in the lithiated/delithiated process. The phase compositions strongly affect the intrinsic properties of the MnO/C nanocomposites, increasing the ion diffusion coefficient from $\sim 10^{-15}$ to 10^{-11} cm^2 s^{-1} when the electrode progressed from the fully charged to fully discharged state, while both the surface redox reaction and the solid-state diffusion could be the limiting process depending on the lithiation/delithiation states. In addition, the MnO/C anode delivers an energy efficiency of 90% in a Li-ion hybrid capacitor, suggesting a promising and competitive application in the future.

Received 3rd January 2019
Accepted 25th February 2019

DOI: 10.1039/c9ta00056a

rsc.li/materials-a

Introduction

Advancements in harvesting renewable energy have been driven by environmental concerns from the utilization of fossil fuels.[1] Energy storage devices have rapidly spread in the forms of smart electronics, electric vehicles, and smart grid stations and have become increasingly indispensable components in modern society. Rechargeable batteries and supercapacitors are the main energy storage devices, in which electrode materials store ions and electrons and convert electricity into chemical energy reversibly in the charge/discharge processes.[2] Electrode materials, in general, store energy through three mechanisms: intercalation, alloying, and conversion.[3,4] Intercalation anode materials always possess working voltage plateaus,[5,6] though the limited active sites in the host lattices restrict the energy densities of full batteries.[7] The alloying materials react with the Li ions to form the alloy phases,[8,9] which leads to rapid pulverization from the typically huge volume expansion.[10,11] The conversion materials are formed through the breakdown and recombination of chemical bonds in the energy storage reactions.[12,13] The theoretical specific capacity and volume expansion of the conversion materials are in between those of the intercalation and alloying materials.[14,15] In transition metal oxides,[16] sulfides,[17] phosphides,[18] and selenides,[19] the metallic transition elements as well as the products consisting of alkaline ions and the anions from the host materials are separated during the discharge processes.

In terms of transition metal oxides, manganese monoxide (MnO) is an ideal material to study the relationship between the structure and electrochemical performance due to its simple cubic crystal structure and its typical voltage profiles with a discharge plateau and sloped charge, similar to those of most oxides.[20–22] MnO holds several advantages as an anode material including a relatively high theoretical specific capacity of 756 mA h g^{-1}, a relatively low discharge voltage around 0.5 V, low cost due to its high abundance in the Earth's crust, and low toxicity. MnO anodes have been extensively studied for improving the rate capability and cycling stability, and the general strategy has been to design the microstructures for increasing the surface area, introducing the conductive network, and tuning the crystallinity.[23–26] For example, MnO nanocrystallites mechanically anchored by pore-surface terminations of graphene-like carbon nanosheets to form a monolayer structure delivered a high specific capacity with good stability, and the Li ion capacitor released a high power density of 15 kW kg^{-1} with 76% capacity retention after 5000 cycles.[27] A

[a]Department of Materials Science and Engineering, University of Washington, Seattle, WA 98195, USA. E-mail: gzcao@uw.edu; jihuiy@uw.edu

[b]Beijing Institute of Nanoenergy and Nanosystems, Chinese Academy of Sciences, Beijing, 100083, China

[c]School of Materials Science and Engineering, North Minzu University, Yinchuan, 750021, China

[d]Shanghai Key Laboratory of Special Artificial Microstructure, Tongji University, Shanghai, 200092, China

† Electronic supplementary information (ESI) available. See DOI: 10.1039/c9ta00056a

topochemical approach was used to synthesize porous MnO/C microspheres by removing $ZnCO_3$ in the mixed carbonates; the high specific capacity of 846 mA h g^{-1} was attributed to the controllable pore sizes.[25] However, some challenges still remain for MnO anodes in storage applications. The formation of interfaces and interphases, and the changes in the chemical bonds of the reactions are complicated. The relationship between the electrochemical diffusion and potential is also important because the diffusion characteristics will affect the rate capability and could create a large potential hysteresis between the charge and discharge voltage profiles, resulting in a significant energy loss.[28] In particular, MnO displays a discharge plateau but also a sloping charge curve of the reverse reaction, similar to most of the transition metal oxides.[24,29] This profile asymmetry between the charge and discharge has a significant effect on the energy efficiency of full batteries.[5]

In this study, MnO was adopted as a model anode to analyze the relationship between the electrochemical potential and electronic structure of the compositions through the crystal field analysis and DFT calculations. MnO/C composites were synthesized using a hydrothermal method with subsequent heat treatment involving an inert gas. Apart from the characterization of the structure and capacitance contribution to the electrochemical performances, cyclic voltammetry (CV) and electrochemical impedance spectroscopy (EIS) were used to monitor the kinetic processes, evolution of charge transfer resistance, and ion diffusion during the charge/discharge processes. On this basis, the change of the interface was analyzed and discussed through simulations of a series of EIS spectra. Moreover, the energy efficiency of the MnO/C anode in a hybrid capacitor has been analyzed to demonstrate its potential use and discern the underlying challenges.

Results and discussion

Electrochemical potential analysis

Fig. 1a shows the potential profiles of the MnO anode, as shown in most of the reported studies.[24,30,31] A potential plateau appears around 0.5 V during the discharge process but during the charging process, a sloping curve is displayed. The conversion reaction of MnO involves the breakdown and recombination of the chemical bonds. The bond dissociation energies have an essential impact on the electrochemical potential along with the electronegativity of the composing elements, which influence the electron distribution and the strength of the chemical bonds. The electron configuration, such as the scheme of Mn(II) in Fig. 1b, determines the order and energy of electrons when they jump into or out of the d or f orbitals during a reaction. MnO works as an anode and decomposes to metallic Mn and Li_2O,

$$MnO + 2Li^+ + 2e^- \leftrightarrow Mn + Li_2O \quad (1)$$

which displays a potential plateau around 0.5 V during the discharge process.[32] Normally, the electrochemical potential is calculated by the Gibbs free energy change in the whole reaction, and the free energy change is defined as[33]

$$\Delta G = \Delta H - T\Delta S = \Delta U + P\Delta V - T\Delta S = -nFE^0 \quad (2)$$

where, the terms $P\Delta V$ from volume change and $T\Delta S$ from configurational change are negligible, as they are of the order of 10^{-5} and 10^{-2} eV, respectively. ΔU is the change in the internal energy, which can be approximated as 2–3 eV to evaluate ΔG in the reaction, when the assumed temperature is 0 K for the DFT calculation.[34] Fig. 1c shows the crystal structures of the materials involved in the conversion reaction of MnO anode, and the lattice parameters are listed in Table S1.† The internal energy of each material including the possible products was calculated by density functional theory, as shown in Table 1. In order to estimate the possibility of the intercalation reaction happening at the beginning, the possible Li–Mn–O compounds were hypothesized and the positive energy changes verify that the intercalation reaction is impossible to occur in the MnO anode. More calculation details are shown in the ESI.† The electrochemical potential (E^0), also called the open circuit voltage (OCV), is calculated by the following equation.

$$E^0 = -[U^{DFT}(Li_2O) + U^{DFT}(Mn) - U^{DFT}(MnO) - 2U^{DFT}(Li)]/2F \quad (3)$$

The calculated E^0 is 1.5 V, which deviates from the reported experimental discharge voltage.[35] The deviation between the experimental and theoretical potentials comes from the theoretical calculation using the open circuit voltage and the experimental reflecting the average. Besides, the configuration entropy was not considered when a new phase nucleated and grew in the host materials, as was the case for the $LiFePO_4$ cathode.[36] Combined with the DFT calculations on the assumed intermediate phases (calculations details in ESI†), the results verify that it is difficult to form the intercalation or alloying phases in the conversion reaction of MnO anode. The chemical bond dissociation energy (BDE) can give an electrochemical potential close to the real state because a conversion reaction involves the breakdown and recombination of chemical bonds. BDE is an enthalpy change but roughly equals the free energy change and could be used to estimate the discharge voltage owing to the negligible volume and configurational change, as mentioned above. The bond energy change in eqn (1) can be calculated using the following equation.

$$\Delta U_{BDE} = (\Delta U_{Mn-Mn} + 2\Delta U_{Li-O}) - (\Delta U_{Mn-O} + 2\Delta U_{Li-Li}) = -nFE_{BDE} \quad (4)$$

The bond dissociation energies for Mn–O, Li–Li, Mn–Mn, and Li–O are 402, 106, 42, and 341 kJ mol^{-1}, respectively.[37] The difference in the bond dissociation energies of the MnO conversion reaction is 110 kJ mol^{-1}, thus, the potential determined by eqn (4) is 0.57 V, which is very close to the experimental value. The slight difference between the experimental and theoretical calculation of the bond energy can be attributed to polarization in the half-cell. However, there is still a large difference between the charging and discharging potential profiles. Most of the transition metal oxides have a visible potential plateau during the discharging process but they

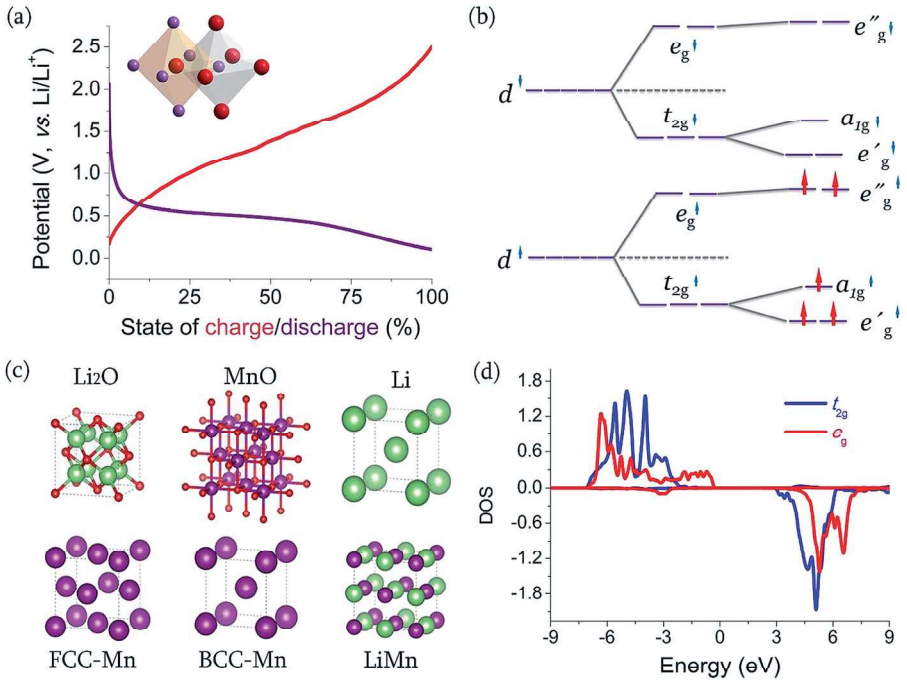

Fig. 1 (a) Voltage profile of the MnO anode in a Li-ion half-cell within the voltage window of 0.01–2.5 V. The discharging voltage profile shows a plateau around 0.5 V *versus* Li/Li^+; however, the charging profile is a sloping curve. The inset is the chemical structure of Mn(II), in which the Mn(II) cation and the O(II) anion are both octahedral. (b) Schematic of the octahedral crystal field splitting. The 3d orbitals in Mn(II) split into two degenerate sets, one containing three orbitals with relatively lower energy, and the other set with two orbitals of relatively higher energy. Five valence electrons occupy the five orbitals separately because the oxygen anion is a weak field ligand. Therefore, it forms a high spin crystal field in MnO. In the DFT calculation, the assumed temperature is 0 K, MnO stays in the antiferromagnetic (AFM) state, and the orbitals go through secondary splitting because the D_{3d} point-group symmetry mixes the t_{2g} so as to show the a_{1c} singlet and e'_g doublet. (c) The crystal structures of L_2O, MnO, metallic Li, FCC-Mn, BCC-Mn, and LiMn for the internal energy and voltage calculations. (d) Density of states of the e_g and t_{2g} orbitals of Mn(II) ion in the AFM state, which is in accordance with the mixed splitting of orbitals in schematic b.

possess sloping profiles that deviate from the calculated results during charging[22,29] due to the electrons jumping in and out of the d or f orbitals, thus causing a change in energy. Manganese (Mn) is a multi-electron atom with 7 valence electrons distributed in the 3d and 4s orbitals, and its metallic state has a cubic structure. The energy level of each orbital influences the electron occupation and the chemical coordination of the cation in its oxides. MnO has a cubic NaCl-type crystal structure, where the Mn^{2+} ion coordinates with six oxygen atoms to form an octahedron (Fig. 1a inset). The remaining five electrons in Mn^{2+} occupy two sets of 3d orbitals with three lower energy t_{2g} orbitals and two higher energy e_g orbitals (Fig. 1b). In the DFT calculation, the assumed temperature is 0 K so that the antiferromagnetic (AFM) MnO has D_{3d} point-group symmetry,[38] leading to a mixed t_{2g} orbital, which shows the a_{1g} singlet and the e'_g doublet as the DOS depicted in Fig. 1d. The invariant e_g is often marked as e''_g in D_{3d} symmetry operations. Since O^{2-} is to a weak-field ligand, it gives rise to a high-spin crystal field in MnO. During the discharging process, MnO transforms to metallic Mn and Li_2O, which suggests the two incoming electrons will jump into the empty e'_g orbitals to reduce Mn^{2+} to the Mn metal. The energy differences for both the electrons are the same, therefore, the potential profiles during the discharging process are plateau-shaped. The belief is that at the beginning of the charging process there are no degenerate orbitals in metallic Mn and the electrons in the 4s orbitals have a higher energy level where the electron cloud overlaps in the 4s and 3d orbitals. In forming MnO, the Mn(II) ion coordinates with an oxygen octahedron and induces the splitting of the 3d orbitals. At this moment, the empty 4s orbitals have a lower energy level than the e'_g orbital, causing the electrons to move from the e'_g to the 4s orbitals. This continuous energy change is manifested as a sloping potential profile during the charging process.[39] A large difference between the charging and discharging potential profiles implies a potential hysteresis that leads to energy losses in a device. The electronegativity of the elements influences the strength of the chemical bonds and affects the potential hysteresis to some extent. Using the electronegativity values, the

Table 1 The internal energy of a cell containing one chemical formula of matter (unit: eV)

MnO	Li	Li_2O	FCC-Mn	BCC-Mn	LiMn	LiMnO	Li_2MnO
−16.406	−1.903	−14.313	−8.900	−8.839	−7.996	−15.811	−17.356

ionic character of the chemical bonds can be evaluated through the following equation,[40]

$$\%\ \text{ionic character} = 1 - 100 \times \exp[-0.25(X_a - X_b)^2] \quad (5)$$

where X_a and X_b are the electronegativity values of the anion and cation, respectively. The electronegativity value of Mn is 1.55 Pauling units and that of O is 3.44 Pauling units. The ionicity in MnO is almost 59.1%, meaning that the ionic bond dominates the chemical properties. Fig. S1† shows the charge density difference map of Mn–O from the DFT calculations. The Mn atoms lose electrons and the O atoms receive electrons to form the Mn–O bond. The electron cloud is denser around the O^{2-} ions and no electron cloud overlapping occurs between Mn and O. The higher ionic character in the chemical bond suggests that the electrons in the 3d orbital have a lower electron sharing tendency, which makes the reaction energetics high.[41] In addition, the Pauling electronegativity of Li is 0.98 and the iconicity of the Li–O bond is almost 78.0%. Thus, the strong ionic bond between the alkaline ions and anions from the transition metal oxides, such as Li_2O, is another possible reason for the electrochemical potential hysteresis. The increase in the energy barriers during the charging process is more than that of the discharge process.[42]

Material characterization

Fig. 2a shows the X-ray diffraction (XRD) patterns of the samples before and after calcination. The sample obtained from the solvothermal synthesis can be indexed with the standard XRD pattern of manganese carbonate ($MnCO_3$, space group $R\bar{3}c$, hexagonal, 4.7901 × 4.7901 × 15.694 Å, PDF card 44-1472), which has a calcite-like structure with Mn(II) exhibiting an octahedral coordination with the anion ligands. More importantly, the formation of the carbonate suggests that glucose was oxidized to the carbonate group during the solvothermal reactions and combined with the Mn cations. The thermogravimetric analysis/differential scanning calorimetry (TGA/DSC) curves reveal the thermal decomposition of $MnCO_3$ in Fig. S2† that displays an endothermal peak at 400 °C, thus implying a decomposition reaction. The drop shown in the TGA curve can be attributed to the release of carbon dioxide. To ensure complete decomposition and good graphitization of the residual carbon, the solvothermal product was calcined at 650 °C for 2 h with nitrogen gas. After the calcination, the main phase transformed into manganese monoxide (MnO, space group $Fm\bar{3}m$, cubic, a = 4.445 Å, PDF card 07-0230), which adopts a rock-salt structure where the cation and anion both have the octahedral coordination (Fig. S3†). The XRD pattern shows peaks corresponding to MnO, as shown in Fig. 2a. The microstructure of the calcined MnO sample looks similar to batches of grass, where the length of a batch is around 1 μm and the diameter is approximately 400 nm (Fig. 2b). All of the batches have uniform size and morphology. Each of them consists of numerous nanoparticles, as revealed by the transmission electron microscopic (TEM) image in Fig. 2c. The center of a single nano-batch is darker than the edges because the center of the three-dimensional batch is thicker in comparison with the edges, so that the electrons are difficult to transmit through it. The local area marked by a green rectangle (Fig. 2d) was magnified, and it was found that crystalline MnO nanoparticles (~6 nm) were encapsulated in the disordered carbon matrix. The apparent lattice fringes, with inter-planar spacing of 2.57 and 2.23 Å, observed by high-resolution transmission electron microscopy (HRTEM) agree with the planar distances of the (111) and (200) in MnO (Fig. 2d). The energy dispersive spectrum was also collected through energy-dispersive X-ray spectroscopy (EDS) attached to the TEM. The elemental composition consisted of Mn, O, and C, which are in accordance with the XRD results and the elements contained in the raw materials. The EDS mappings in Fig. 2f–h present the elemental distribution consistent with the batch-like particle shape in Fig. 2c. The carbonization of glucose provides the final carbon network in the calcined sample. Raman spectrum of the sample was collected; the peak fitting was conducted with the Gaussian function for the D- and G-bands and the Lorentzian function for the additional I and D″ bands (Fig. 2i). The D-band located around 1339 cm^{-1} originates from a double resonance process involving a phonon and a defect, which implies that the carbon is disordered. The G-band at ~1589 cm^{-1} stems from the in-plane vibrations and has the E_{2g} symmetry that denotes the graphitization of carbon. The I band at ~1180 to 1290 cm^{-1} relates to the disorder in the graphitic lattice, which can be attributed to the sp^2–sp^3 bonds or the presence of polyenes. The D″ band at ~1500 cm^{-1}, associated with interstitial defects in the disordered sp^2 bonds, implies that the carbon is amorphous.[43,44] The ratio of the intensity between the D- and the G-band (I(D)/I(G)) is 0.94, which suggests that the carbon in the calcined sample is in an amorphous state. The carbon content obtained from the DSC/TG curves is 25.5% (Fig. S4†) and the electrical conductivity determined by a four-point probe direct current technique is 106 S m^{-1}, which is enough to ensure that the charges are transferred in the electrochemical reactions. Additionally, the nitrogen adsorption isotherm was used to determine the specific surface area through the Barrett–Joyner–Halenda (BJH) method, which was found to be 202.2 m^2 g^{-1} with the pore size distribution peak appearing at 4 nm (Fig. 2j). The hysteresis loop between the adsorption and desorption branches implies that capillary condensation occurred within the mesoporous structure. Assuming that the MnO nanoparticles have a spherical shape with a diameter of 6 nm and the theoretical density of MnO is 5.36 g cm^{-3}, the calculated surface area should be 93.2 m^2 g^{-1}. The large difference between the experimental and calculated values suggests that the batch-like MnO/C has porous nanostructures. We speculate that this is because the decomposition of $MnCO_3$ releases CO_2, which helps to produce more pores in the carbon coating and more MnO nanoparticles during the calcination process.

Lithiation kinetics and diffusivity

As described in the characterization section, MnO/C nanocomposite presents a high electrical conductivity of 106 S m^{-1}, so no conductive additive was added in preparing the electrode in the electrochemical property test and battery performance

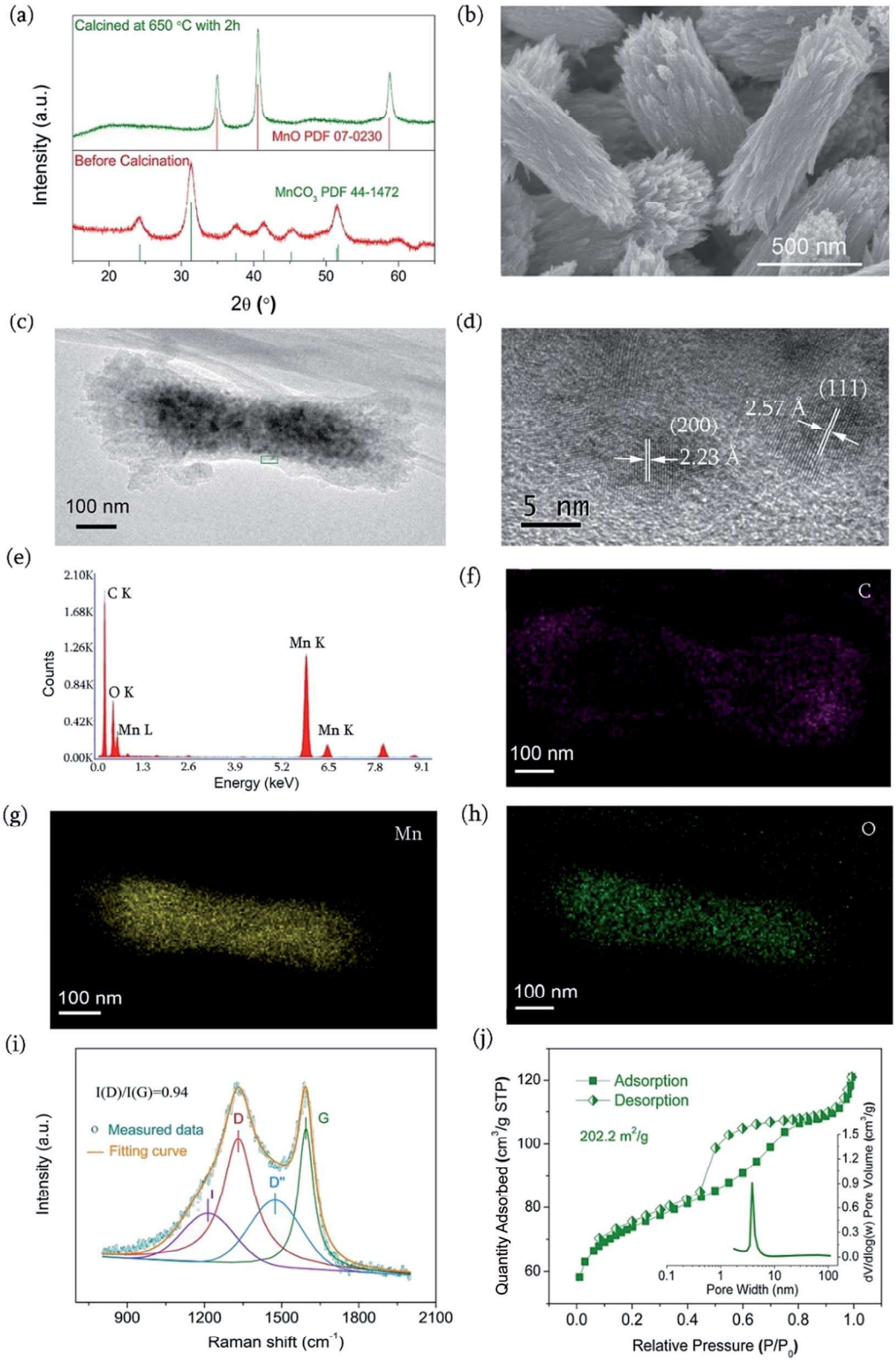

Fig. 2 (a) XRD patterns of the sample before and after calcination. The sample derived from the solvothermal synthesis is rhodochrosite $MnCO_3$ and it transforms to the rock salt structure after calcination at 650 °C. (b) SEM image of the calcined sample MnO/C that grows in a batch-like shape. (c) TEM image of a single batch-like nano-particle, and (d) HRTEM image from a local area of the single particle. The lattice spacings verify the structure of MnO/C. (e) EDS spectrum collected from the single batch particle. The existing elements (Mn, O, C) are in accordance with the raw materials. Carbon stems from the added glucose in the synthesis process (f–h) EDS mapping of C, Mn, and O. All of the elements are distributed homogenously within the whole particle. (i) Raman spectrum of the MnO particles. The D, G, I, and D″ bands reflect the graphitization

characterization and analyses. The redox characteristics of MnO/C were tested through a cyclic voltammogram (CV) within a working voltage window of 0.01–3.00 V and at a sweeping rate of 0.1 mV s^{-1}. The CV curves (Fig. 3a) show a reducing peak at 0.29 V in the first cycle, which shifts to 0.35 V in the following cycles. In this process, the Mn–O bonds break down and MnO transforms into Mn and Li_2O. In the reverse process, the oxidizing peaks at 1.22 V overlap during the first three cycles, suggesting that MnO was recovered and there is good reactive reversibility in the MnO/C anode. The CV curves at various sweeping rates (Fig. S5a†) were also collected to analyze the kinetic characteristics of the MnO/C nanocomposite during the lithiation/delithiation processes because nanomaterials always have high specific surface areas that endow the reaction kinetics with a simultaneous diffusion- and capacitance-controlled process.[45–47] The diffusion component relates to the faradaic reaction from the Li^+ insertion process, which always occurs in the intercalation, alloying, or conversion reaction. The capacitance component corresponds to the surface faradaic reaction, which can be thought of as that seen for a pseudocapacitor and the non-faradaic reaction from the electric double layer capacitance.[48,49] Both of the latter capacitive contributions can be separated by analyzing the various sweeping rates of the CV curves because the measured current i obeys a power law relationship with the sweeping rate υ[49,50] as,

$$i = a\upsilon^b \tag{6}$$

where a and b are the adjustable parameters, and the b-value can be calculated from the log i *vs.* log υ plot (Fig. S5b and c†). A b-value close to 0.5 means that the current primarily stems from the faradaic diffusion-controlled process, and a b-value of 1.0 implies a capacitance-controlled process from the surface reactions.[45] Fig. 3b shows the b-values calculated from the log i − log υ relationship at different states of charge/discharge, and it is easily concluded that the b-value varies with the state of the electrode. In the discharge process, surface adsorption and faradaic reaction happen when the voltage is higher than 2 V, so that the b-value is close to 1. In this case, the whole process is controlled by ion adsorption onto the surface of the electrode material due to its high surface area, as verified by the nitrogen sorption isotherm tests. The conversion reaction starts at 1.5 V and the Li ions migrate across the interfaces between the carbon coating and MnO nanoparticles, thus, the b-value is around 0.51. The b-values in the voltage window of 0.5–0.8 V lie around 0.75, suggesting that the Li ions are adsorbed and diffuse across the surface of the MnO nanoparticles. A b-value of 0.49 around 0.3 V signifies a strong diffusion-controlled process related to the breakdown of the chemical bonds, as verified by the CV curve (Fig. 3a). After the breakdown of the chemical bonds, the b-value sits between 0.5 and 1.0, implying that charge storage is simultaneously affected by the surface adsorption effect from the porous batch-like nanostructure as well as the diffusion-limited faradaic reaction from the MnO nanoparticles inside. On being charged back to 0.3 V, the b-value becomes 0.51, signifying the start of the recombination of Mn and O and the diffusion-controlled reaction process. In the subsequent charging process, the b-values fall within the range of 0.5–1.0, which suggests a mixed contribution from the diffusion and capacitance processes. The diffusion-controlled influence stems from the conversion reaction of MnO, and

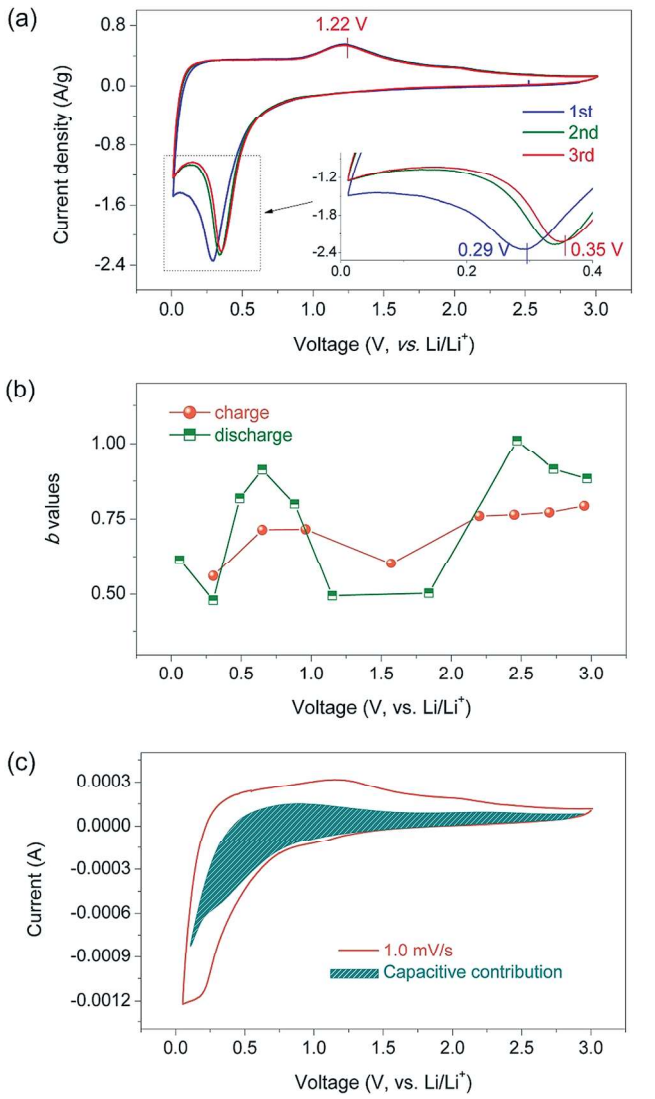

Fig. 3 (a) Cyclic voltammetric curve of the MnO/C anode without the addition of conductive material in a Li-ion half cell, where the Li metal was used as the counter electrode. The reducing peak around 0.35 V and the oxidizing peak at 1.22 V represent the conversion reaction of the MnO/C anode in the discharging and charging process, respectively. (b) b-values at various voltages. The data were calculated from the CV curves at varying sweep rates and used to evaluate the diffusion or adsorption-controlled reaction process at different electrochemical stages. (c) The separated capacitive contribution (shaded area) of the total charge storage at a sweeping rate of 1 mV s^{-1}. The capacitive contribution is around 60% of the total energy storage state.

or disordered state of carbon in the calcined sample (j) Nitrogen sorption isotherm of MnO/C and the pore size distribution. The hysteresis loop in the curves suggests that the batch-like MnO particles contain abundant mesopores.

the capacitance-controlled contribution originates from the surface and interface of the nanostructured MnO/C. A relatively low *b*-value appears at 1.6 V during the charging process, which corresponds to the interface diffusion between the carbon coating and MnO. The interface between the two phases induces the ion accumulation or the double-layer effect storage generated from different ion diffusion rates at the same electric field. From the work of Dunn and his coworkers, the capacitance contribution can be separated from the CV curves because the current (i) at a fixed voltage (V) equals to the sum of the capacitive effect ($k_1\upsilon$) and diffusion-controlled contribution ($k_2\upsilon^{1/2}$), as described below.[50]

$$i(V) = k_1\upsilon + k_2\upsilon^{1/2} \quad (7)$$

Fig. 3c shows that the capacitance contribution approaches 60% in the CV curve at a sweeping rate of 1.0 mV s^{-1}, revealing a strong capacitive effect in the nanostructured MnO/C electrode. The large surface area is a possible reason for the high capacitance contribution due to the formation of an electric double layer between the electrolyte and the carbon coating. Since MnO is a semiconductor and carbon is a conductor, the interface between them easily becomes a charge region to store the charges, just as in the capacitors.[51] However, this capacitance effect is weak in comparison to that between the electrode and electrolyte. The rate capability of the batch-like MnO/C anode was tested in a half cell where lithium metal was used as the counter electrode and the testing voltage window was 0.01–2.50 V (Fig. S6a†). The first discharge capacity reaches 1215 mA h g^{-1} and the subsequent capacity stabilizes at 1018 mA h g^{-1} at a current density of 0.2 A g^{-1}, which are both higher than the theoretical value of 756 mA h g^{-1}, due to the formation of a reversible solid electrolyte interphase (SEI) and the capacitance contribution from the interfaces, as reported in the literature.[27,52–54] Normally, the SEI formed on the graphite particle's surface prevents the co-intercalation of the organic solvent molecules so as to suppress the exfoliation of the graphite flake and consumption of the electrolyte to enhance the cyclic stability in subsequent cycles.[55,56] However, the poly/gel-like SEI film in the transition metal oxide anode is reversible owing to the probable catalytic effect from the oxides, and provides an extra capacity in the low voltage region.[53,54] More details will be further discussed in the following EIS analysis. As the current density increases to 6.4 A g^{-1}, the electrode still delivers a specific capacity of 256 mA h g^{-1}, which is higher than most of the reported results[57,58] with no conductive carbon added to the electrode. The cycling stability of the electrode was also tested at a current density of 0.8 A g^{-1}. The specific capacity reaches 594 mA h g^{-1} and the capacity retention of 80% was observed over 200 cycles (Fig. S6b†). Table S2† compares the electrochemical performances of the reported MnO anodes with our results. The good rate capability and cycling stability in our work can be ascribed to the improved kinetics, which means a shortened ion diffusion path and accelerated charge transfer in the MnO/C composite. For example, the small 6 nm size of the active MnO nanoparticles benefits the diffusion-controlled processes. The high specific surface area increases the ion exchange sites and the reaction rate. The porous batch-like nanostructure with interconnected 3-D conductive network ensures excellent charge transfer. All of these effects synergistically improve the reaction kinetics of the MnO/C anode and increase its performance in the Li-ion half cells.

In order to further understand the details of the MnO/C anode kinetics, especially the ion diffusion and charge transfer in the charge/discharge process, EIS was adopted to record the change in the impedance spectra at different electrochemical states in the 3rd cycle. The galvanostatic current density was set at 20 mA g^{-1} to ensure that the reactions achieved equilibrium. The cell was allowed to rest for 20 min before collecting the EIS spectra at a voltage amplitude of 5 mV. Fig. 4a shows the EIS spectra during the discharging process. Initially, the spectrum at 2.4 V consists of a semicircle at high frequency and a subsequent straight line at lower frequency. Before the voltage decreases below 1.2 V, all the spectra are similar in shape, though the slope of the straight line is slightly different. However, there were two semicircles present when the voltage was lower than 1.0 V. The diameters of the semicircles gradually decrease when the voltage goes down. At 0.2 V, the spectrum displays the smallest two semicircles with a straight line. During the charging process, the spectra evolve from two semicircles with a linear tail to one semicircle and a linear tail (Fig. S7a†). The charging spectra at fixed voltages exhibit similar shapes and sizes as the results in the discharging spectra, thus demonstrating good reversibility of the electrochemical reactions in the MnO/C electrode. In general, the EIS spectrum can be fit with an equivalent circuit that includes the resistance of the electrolyte (R_s), the resistance of the SEI film (R_f), charge transfer resistance (R_{ct}), constant phase element (CPE), and the Warburg resistance (Z_W). The Li-ion diffusion coefficients of the electrodes can be calculated from the low-frequency plots of the EIS spectra, based on the following equations,[39]

$$Z' = R_s + R_f + R_{ct} + \sigma_w\omega^{-0.5} \quad (8)$$

$$D_{Li^+} - R^2T^2/2A^2n^4F^4C^2\sigma_w^2 \quad (9)$$

where ω, A, n, F, C, R, and T stand for the angular frequency, electrode area (0.50 cm^2), reactive electron number per chemical formula (2), Faraday's constant (96 500 C mol^{-1}), the molar concentration of Li ions (1.0×10^{-3} mol cm^{-3}), gas constant (8.314 J mol^{-1} K^{-1}), and the testing temperature (298 K), respectively. It is worth noting that the Li-ion concentration was assumed to be same as that of the electrolyte and stayed constant owing to the fact that the Li metal anode provided sufficient Li ions for the electrochemical reaction. The Warburg coefficient (σ_w) was obtained from the slopes of the Z'–$\omega^{-1/2}$ curves, as shown in Fig. S7b and c.† The ion diffusion coefficients are shown in Fig. 4b. At different stages of charge/discharge, the MnO/C electrode has different ion diffusion coefficients. The fully charged state at 3.0 V has the lowest coefficient of ~10^{-15} cm^2 s^{-1} and the fully discharged state at 0.01 V has the highest coefficient of ~10^{-11} cm^2 s^{-1}, which is higher than the commercial and other nanostructured MnO at the same voltages. This is due to the smaller particle size (~6

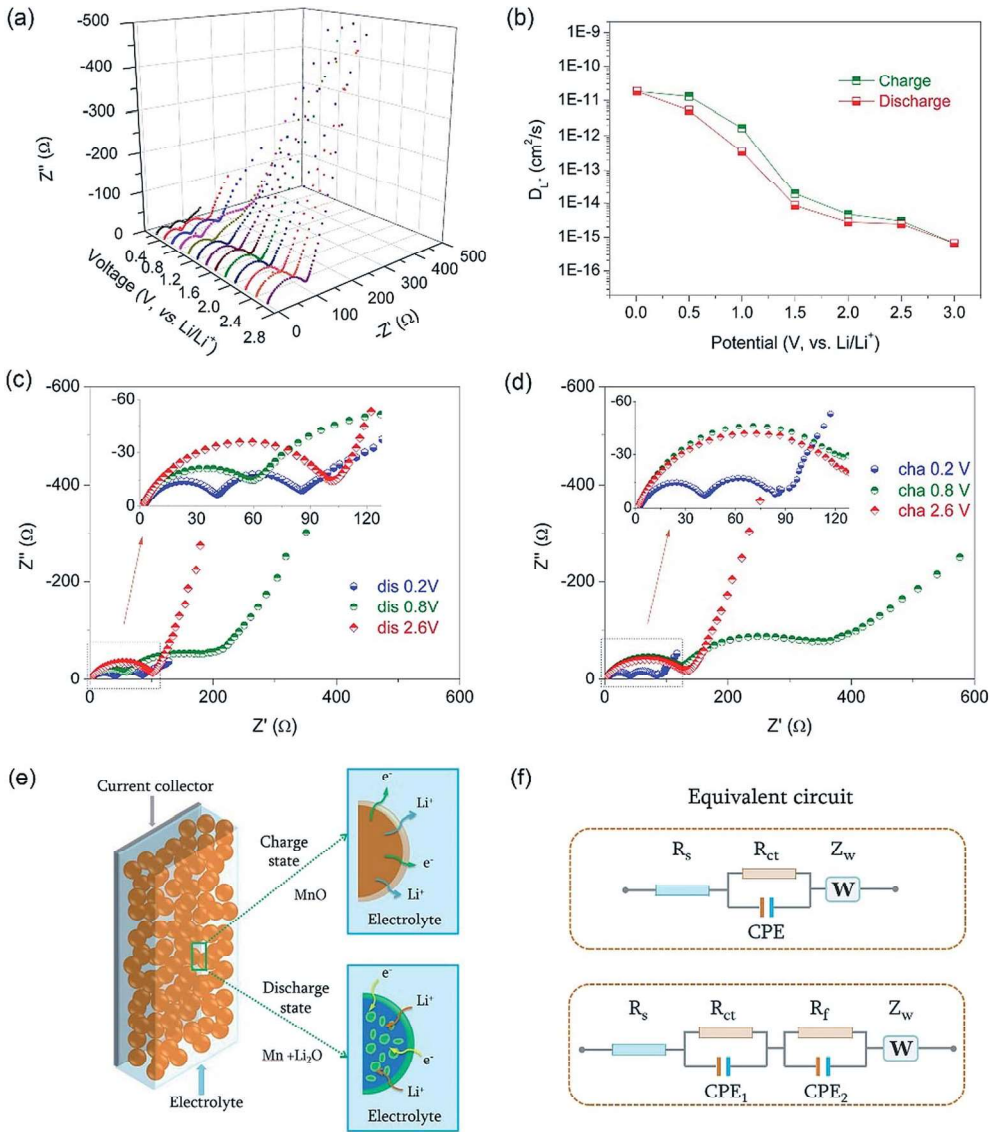

Fig. 4 (a) Electrochemical impedance spectra at different discharge stages. The semicircle changes from one to two when the potential decreases from a fully charged state (3.0 V) to a fully discharged state (0.01 V). (b) The Li-ion diffusion coefficients of the MnO/C anode under different electrochemical potentials. The difference between the coefficient of the fully charged and discharged states stems from the varying phase compositions. (c) A comparison of the EIS spectra at different discharge potentials *versus* Li/Li^+. The resistances from the semicircles present a remarkable variation, especially when the formation of the solid electrolyte interphase starts around 0.8 V owing to the decomposition of the electrolyte. (d) EIS spectra at various charging stages. The resistances at 0.8 V increase more than that collected at a discharging state, implying a reaction hysteresis between the charging and discharging states at the same electrochemical potential. (e) Schematic of the phase transition and composition of the charging and discharging states. The formation of a SEI and the precipitation of the metallic Mn change the chemical compositions and states of the whole electrode. (f) The equivalent circuit for EIS spectra at different states. An additional circle in the EIS suggests a parallel resistance (*R*) and constant phase element (CPE) in the equivalent circuit and a new interphase is formed in the electrode.

nm) of MnO and higher electrical conductivity (106 S m^{-1}) of the carbon coating in comparison with other nanostructured MnO composites, such as mesocrystal MnO that has a particle size of around 10 nm and electrical conductivity of 2.97×10^{-3} S cm^{-1}.[39] Furthermore, the charged state at a fixed voltage displays a slightly higher coefficient than that of the discharged state. The possible reason for the large coefficient difference at fully charged and discharged states can be attributed to the phase compositions of the MnO/C electrode. In the fully charged state, the phase is cubic MnO, which has a strong ionic chemical bond (Mn–O, 402 kJ mol^{-1})[37] and a high atomic packing density (~68%), making it difficult for the Li-ion to diffuse through the crystal body. However, in the fully discharged state, there are metallic Mn and Li_2O. Aside from the relatively weak chemical bond of Li–O (341 kJ mol^{-1}),[37] the products in the fully discharged state are in the amorphous state or local short-range ordered arrangement,[31,52] meaning they are loosely packed. Thus, the working ions can easily migrate through the open spaces or channels. The EIS spectra at 0.2, 0.8, and 2.6 V in the charge/discharge states are plotted

together to compare and analyze the effects of the phase compositions in the electrode (Fig. 4c–d). A schematic of the phase evolution and equivalent circuits is shown in Fig. 4e–f. During the initial discharge process, the phase at 2.6 V is MnO and the semicircle in the EIS spectrum stems from the resistance (104 Ω) corresponding to the charge transfer in MnO, which agrees with the reported MnO anode behavior in the charging state.[24,52,59] When the voltage decreases to 0.8 V, two semicircles appear as per the literature.[60] The one at the higher frequency still relates to the charge transfer resistance (60 Ω) but the other semicircle of lower frequency correlates to the resistance from the SEI film (145 Ω). Based on the brick-layer model,[61] the capacitances of the nanoparticles (CPE1) is far smaller than the capacitances from the interfaces between the SEI and MnO particles (CPE_2) because the width of the interface is smaller than the particle size. The simulated results listed in Table 2 strongly support this argument. The increase of the resistance at 0.8 V can be attributed to the formation of a SEI accompanied by the decomposition of the electrolyte and the breakdown of MnO. Additionally, the disordered atoms scatter the charges, leading to an increase in the resistance. At the discharge state of 0.2 V, both resistances became smaller. The possible reason for this is that the metallic Mn precipitates homogenously to form a conductive network in the electrode. Additionally, the composition of the SEI gradually changes, benefiting the formation of Li_2CO_3 by increasing the charge transfer and ion migration but decreasing the LiF formation owing to its insulating property.[62–64] In the reverse charging process, similar EIS spectra at 0.2 V with the comparable resistances at the discharge state of 0.2 V was obtained, indicating the similar chemical surroundings in the electrode. When the voltage increases to 0.8 V, the R_{ct} and R_f are larger than those at the same discharge state. The possible reason is that the partial decomposition of the SEI and Li_2O leads to the disappearance of the electronic and ionic components, resulting in the increased resistances. LiF, which is an electronic insulator, needs a high decomposition voltage of 6.1 V to break its strong ionic bond if the system cannot provide enough driving force.[65] When charged to 2.6 V, the R_{ct} is around 126 Ω, which is higher 104 Ω at the same discharge voltage, thus suggesting that a slightly high-resistance component remains in the system or a slight change on the particle surface that is not fully recovered. The similar EIS spectra under the same charge and discharge voltage and the change in the number of semicircles under different voltage suggest a nearly reversible SEI owing to the fact that the capacitances from the SEI appear and then disappear in the discharge and charge process. The reason is that the compositions of the SEI and the electrode materials have different dielectric constants that lead to a large difference in the capacitances, as shown in Table 2. In the charge process, the second semicircle in the middle frequency region disappears, meaning that one interface disappears. In fact, the solid electrode material that cannot disappear probably corresponds to the SEI layer. This reversible SEI plays a role in the ion and electron storage reservoir that allows for the high specific capacity and ensures a stable cycling performance. The gradually increasing ion diffusion coefficient during the discharge process accelerates the electrode reactions and enhances the rate capability. It is worth noting that the nanostructured MnO/C anode still favors high ion migration but the reaction is controlled by diffusion at low voltages such as 0.3 V.

Table 2 The resistances (R_s, R_{ct}, and R_f) and capacitances (CPE1, CPE2)

States	Voltage (V)	R_s (Ω)	R_{ct} (Ω)	R_f (Ω)	CPE1 (F)	CPE2 (F)
Discharge	2.6	2.5	104	—	2.13×10^{-5}	—
	0.8	2.6	66	173	3.01×10^{-5}	1.68×10^{-3}
	0.2	2.5	42	53	3.12×10^{-5}	1.57×10^{-3}
Charge	0.2	2.3	44	53	4.70×10^{-5}	1.82×10^{-3}
	0.8	2.7	135	234	1.49×10^{-5}	9.35×10^{-4}
	2.6	2.5	142	—	5.00×10^{-5}	—

Performances in the Li-ion capacitor

The electrochemical potential and diffusivity of the electrode materials have significant impact on the performances of a device, especially the energy density and efficiency. Choosing a stable cathode with a slight or no voltage hysteresis can effectively reveal the true performance of MnO/C in a full cell. Activated carbon (AC) has excellent chemical stability and a high specific surface area, therefore it is generally used in electrodes for supercapacitors.[66] A commercial AC derived from coconut shell with a specific surface area around 1800 $m^2\ g^{-1}$ was adopted as a cathode to build a Li-ion capacitor with MnO/C as the anode (Fig. 5a). A Celgard polymer film and packaged porous Li metal foil was used to separate the cathode and anode, to compensate for the Li consumption during the first lithiation of the MnO/C anode, and to avoid the complex process of preparing a pre-lithiated anode and an assembly capacitor in two steps.[67] In the half cells, the AC cathode has a maximum voltage of 4.5 V and the MnO/C anode reaches a minimum voltage of 0.01 V *versus* Li/Li^+ (Fig. 5b). Taking into consideration the discharge voltage plateau of the MnO/C anode around 0.5 V, the working window of the capacitor was set to 0.1–4.0 V. The capacitor ran over 20 cycles at a current density of 0.1 A g^{-1} to activate the anode (Fig. 5c). The initial capacity was 405 mA h g^{-1} with a coulombic efficiency of 75%, meaning that the lithiation of the anode consumed Li ions to form a SEI. In the following cycles, the coulombic efficiency stayed at 100% and the specific capacity slightly increased. Even when the current density increased to 25.6 A g^{-1}, the capacitor still delivered a specific capacity of 57 mA h g^{-1} within 9 s, reaching a high-power density of 11 160 W kg^{-1}. When the current density returned to 0.1 A g^{-1}, the capacity was very similar to the initial capacity. The capacitor was cycled at 5 A g^{-1} for 1000 cycles; the specific capacity remained at around 300 mA h g^{-1} and displayed an undetected degradation during the long-term cycling process (Fig. 5d). This excellent cycling stability exhibits a huge competitive advantage in comparison to the reported Li-ion capacitors such as the VN//AC,[68] MnO//CNS,[27] and TiC//AC[69] systems. The energy efficiency of the Li-ion

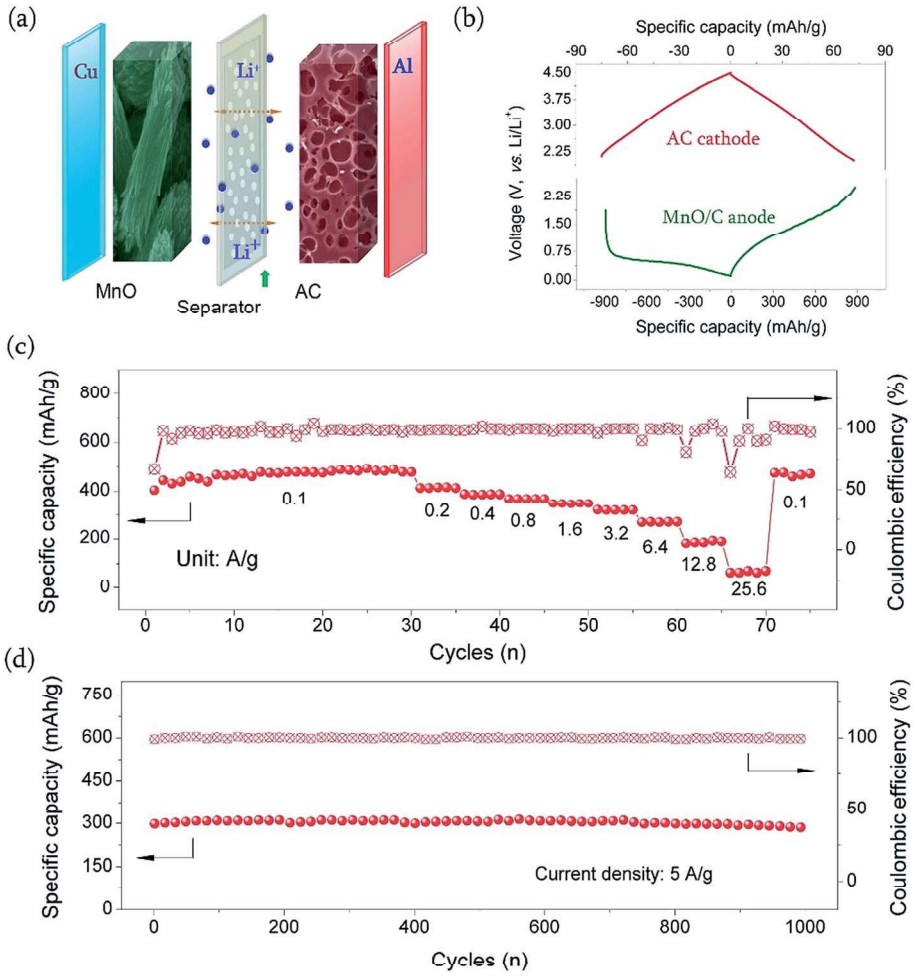

Fig. 5 (a) Schematic configuration of the hybrid Li-ion battery. The MnO/C anode and activated carbon cathode is separated by a Celgard polymer separator and packaged porous Li metal for compensating the Li ion consumption of the anode during the first cycles. (b) The voltage profiles of both the electrodes and their working windows. The voltage difference between the cathode and anode is the maximum voltage window of the full capacitor. (c) The rate capability of the MnO/C//AC hybrid capacitor within a working voltage window of 0.1–4.0 V. The capacitor at 25.6 A g^{-1} can deliver a power density of 11 160 W kg^{-1} within 9 s. (d) The cycling stability of the hybrid capacitor at a current density of 5 A g^{-1} shows no degradation over 1000 cycles.

batteries is defined as the ratio between the discharge and charge energy densities.[70] The energy efficiency of the MnO/C// AC capacitor reaches 90% at a current density of 0.1 A g^{-1}, which is slightly lower than the value of 95% for the $Li_3V_2(PO_4)_3$//$Li_4Ti_5O_{12}$ battery.[70] The reason for the lower energy efficiency stems from the voltage polarization of the anode because the discharge energy density of the capacitor is the area encompassed by the charge voltage curve of the anode and the discharge voltage curve of the cathode.[5] This work shows that discovering the reasons behind the voltage profiles is valuable for designing desirable electrode materials and fabricating high-efficiency energy storage devices.

Conclusions

The thermodynamical calculation and the crystal field analysis revealed that the bond dissociation energy correlates with the discharge potential of MnO. The different electron ordering of the split 3d orbitals determines the potential profiles and the energy difference from the t_{2g} and e_g orbitals leads to the potential hysteresis in the charge/discharge process. For the MnO/C anode, the diffusion and surface reaction contribution were found to vary significantly at different charge/discharge states; Li ion diffusion coefficient changed from $\sim 10^{-15}$ cm^2 s^{-1} at the fully charged state to $\sim 10^{-11}$ cm^2 s^{-1} at the fully discharged state. The continuously changing phase compositions, especially the precipitated Mn and partially amorphous oxide, are likely to reduce the charge transfer resistance and enhance the ion migration during the discharging process. The high specific surface area and smaller size of the MnO/C nanostructures allowed us to achieve high reversible capacity of 1018 mA h g^{-1} with the capacitance contribution of around 60%, and an energy storage efficiency of 90% was attained in the MnO/C//AC capacitor. These fundamentals of ionic diffusion and electrochemical potential, and the practical example are helpful

to understand a given material and to design and/or tune a desired material for highly efficient energy storage.

Conflicts of interest

There are no conflicts to declare.

Acknowledgements

This work was supported by the National Science Foundation (DMR No. 1505902, No. 1803256). Part of this work was conducted at the Molecular Analysis Facility, a National Nanotechnology Coordinated Infrastructure site at the Clean Energy Institute in the University of Washington (Grant ECC1542101).

References

1 D. Larcher and J. M. Tarascon, *Nat. Chem.*, 2015, 7, 19–29.
2 J. B. Goodenough, *Energy Storage Materials*, 2015, **1**, 158–161.
3 H. D. Yoo, E. Markevich, G. Salitra, D. Sharon and D. Aurbach, *Mater. Today: Proc.*, 2014, **17**, 110–121.
4 S. Goriparti, E. Miele, F. De Angelis, E. Di Fabrizio, R. Proietti Zaccaria and C. Capiglia, *J. Power Sources*, 2014, **257**, 421–443.
5 C. Liu and G. Cao, in *Nanomaterials for Energy Conversion and Storage*, ed. D. Wang and G. Cao, WORLD SCIENTIFIC (EUROPE), 2018, DOI: 10.1142/9781786343635_0010, pp. 397–451.
6 N. Nitta, F. Wu, J. T. Lee and G. Yushin, *Mater. Today: Proc.*, 2015, **18**, 252–264.
7 R. C. Massé, C. Liu, Y. Li, L. Mai and G. Cao, *Natl. Sci. Rev.*, 2017, **4**, 26–53.
8 M. Ashuri, Q. R. He and L. L. Shaw, *Nanoscale*, 2016, **8**, 74–103.
9 S. Wu, C. Han, J. Iocozzia, M. Lu, R. Ge, R. Xu and Z. Lin, *Angew. Chem., Int. Ed.*, 2016, **55**, 7898–7922.
10 N. Nitta and G. Yushin, *Part. Part. Syst. Charact.*, 2014, **31**, 317–336.
11 M. N. Obrovac and V. L. Chevrier, *Chem. Rev.*, 2014, **114**, 11444–11502.
12 P. Poizot, S. Laruelle, S. Grugeon, L. Dupont and J. M. Tarascon, *Nature*, 2000, **407**, 496–499.
13 F. Wang, S. W. Kim, D. H. Seo, K. Kang, L. Wang, D. Su, J. J. Vajo, J. Wang and J. Graetz, *Nat. Commun.*, 2015, **6**, 6668.
14 J. Cabana, L. Monconduit, D. Larcher and M. R. Palacín, *Adv. Mater.*, 2010, **22**, E170–E192.
15 F. Wu and G. Yushin, *Energy Environ. Sci.*, 2017, **10**, 435–459.
16 M. V. Reddy, G. V. S. Rao and B. V. R. Chowdari, *Chem. Rev.*, 2013, **113**, 5364–5457.
17 Y. Xiao, S. H. Lee and Y. K. Sun, *Adv. Energy Mater.*, 2017, 7, 1601329.
18 X. Wang, H. M. Kim, Y. Xiao and Y. K. Sun, *J. Mater. Chem. A*, 2016, **4**, 14915–14931.
19 T. Lu, S. M. Dong, C. J. Zhang, L. X. Zhang and G. L. Cui, *Coord. Chem. Rev.*, 2017, **332**, 75–99.
20 L. Liu, X. Yang, C. Lv, A. Zhu, X. Zhu, S. Guo, C. Chen and D. Yang, *ACS Appl. Mater. Interfaces*, 2016, **8**, 7047–7053.
21 K. Adpakpang, X. Jin, S. Lee, S. M. Oh, N. S. Lee and S. J. Hwang, *ACS Appl. Mater. Interfaces*, 2016, **8**, 13360–13372.
22 W. Eom, A. Kim, H. Park, H. Kim and T. H. Han, *Adv. Funct. Mater.*, 2016, **26**, 7605–7613.
23 Y. Sun, X. Hu, W. Luo, F. Xia and Y. Huang, *Adv. Funct. Mater.*, 2013, **23**, 2436–2444.
24 H. Jiang, Y. Hu, S. Guo, C. Yan, P. S. Lee and C. Li, *ACS Nano*, 2014, **8**, 6038–6046.
25 K. Su, C. Wang, H. G. Nie, Y. Guan, F. Liu and J. T. Chen, *J. Mater. Chem. A*, 2014, **2**, 10000–10006.
26 C. Liu, C. Zhang, H. Song, X. Nan, H. Fu and G. Cao, *J. Mater. Chem. A*, 2016, **4**, 3362–3370.
27 H. L. Wang, Z. W. Xu, Z. Li, K. Cui, J. Ding, A. Kohandehghan, X. H. Tan, B. Zahiri, B. C. Olsen, C. M. B. Holt and D. Mitlin, *Nano Lett.*, 2014, **14**, 1987–1994.
28 S.-H. Yu, X. Feng, N. Zhang, J. Seok and H. D. Abruña, *Acc. Chem. Res.*, 2018, **51**, 273–281.
29 W. M. Zhang, X. L. Wu, J. S. Hu, Y. G. Guo and L. J. Wan, *Adv. Funct. Mater.*, 2008, **18**, 3941–3946.
30 X. Jiang, W. Yu, H. Wang, H. Xu, X. Liu and Y. Ding, *J. Mater. Chem. A*, 2016, **4**, 920–925.
31 M. M. Butala, K. R. Danks, M. A. Lumley, S. Zhou, B. C. Melot and R. Seshadri, *ACS Appl. Mater. Interfaces*, 2016, **8**, 6496–6503.
32 K. Zhong, X. Xia, B. Zhang, H. Li, Z. Wang and L. Chen, *J. Power Sources*, 2010, **195**, 3300–3308.
33 G. Yoon, D. H. Kim, I. Park, D. Chang, B. Kim, B. Lee, K. Oh and K. Kang, *Adv. Funct. Mater.*, 2017, **27**, 1702887.
34 C. Liu, Z. G. Neale and G. Cao, *Mater. Today: Proc.*, 2016, **19**, 109–123.
35 H. Li, P. Balaya and J. Maier, *J. Electrochem. Soc.*, 2004, **151**, A1878–A1885.
36 J. Gao, S. Q. Shi and H. Li, *Chin. Phys. B*, 2016, **25**, 018210.
37 J. G. Speight, *Lange's Handbook of Chemistry, 70th Anniversary Edition*, McGraw-Hill Professional, 16th edn, 2005.
38 G. Trimarchi, Z. Wang and A. Zunger, *Phys. Rev. B*, 2018, **97**, 035107.
39 C. Liu, C. Zhang, H. Song, C. Zhang, Y. Liu, X. Nan and G. Cao, *Nano Energy*, 2016, **22**, 290–300.
40 W. D. Callister, *Fundamentals of Materials Science and Engineering*, John Wiley & Sons, Inc., 2001.
41 C. Liu, C. Zhang, H. Fu, X. Nan and G. Cao, *Adv. Energy Mater.*, 2017, **7**, 1601127.
42 X. Nan, C. Liu, K. Wang, W. Ma, C. Zhang, H. Fu, Z. Li and G. Cao, *Journal of Materiomics*, 2016, **2**, 350–357.
43 Y. Zhou, S. L. Candelaria, Q. Liu, Y. Huang, E. Uchaker and G. Cao, *J. Mater. Chem. A*, 2014, **2**, 8472–8482.
44 T. Jawhari, A. Roid and J. Casado, *Carbon*, 1995, **33**, 1561–1565.
45 T. Brezesinski, J. Wang, J. Polleux, B. Dunn and S. H. Tolbert, *J. Am. Chem. Soc.*, 2009, **131**, 1802–1809.
46 Y. Zhu, L. Peng, D. Chen and G. Yu, *Nano Lett.*, 2016, **16**, 742–747.
47 S. Huang, L. Zhang, X. Lu, L. Liu, L. Liu, X. Sun, Y. Yin, S. Oswald, Z. Zou, F. Ding and O. G. Schmidt, *ACS Nano*, 2017, **11**, 821–830.

48 B. E. Conway, V. Birss and J. Wojtowicz, *J. Power Sources*, 1997, **66**, 1–14.
49 J. Wang, J. Polleux, J. Lim and B. Dunn, *J. Phys. Chem. C*, 2007, **111**, 14925–14931.
50 H. S. Kim, J. B. Cook, H. Lin, J. S. Ko, S. H. Tolbert, V. Ozolins and B. Dunn, *Nat. Mater.*, 2017, **16**, 454–460.
51 J. Mei, T. F. Yi, X. Y. Li, Y. R. Zhu, Y. Xie and C. F. Zhang, *ACS Appl. Mater. Interfaces*, 2017, **9**, 23662–23671.
52 Y. Xia, Z. Xiao, X. Dou, H. Huang, X. Lu, R. Yan, Y. Gan, W. Zhu, J. Tu, W. Zhang and X. Tao, *ACS Nano*, 2013, **7**, 7083–7092.
53 S. Laruelle, S. Grugeon, P. Poizot, M. Dollé, L. Dupont and J.-M. Tarascon, *J. Electrochem. Soc.*, 2002, **149**, A627–A634.
54 A. Ponrouch, P.-L. Taberna, P. Simon and M. R. Palacín, *Electrochim. Acta*, 2012, **61**, 13–18.
55 G. C. Chung, H. J. Kim, S. I. Yu, S. H. Jun, J. w. Choi and M. H. Kim, *J. Electrochem. Soc.*, 2000, **147**, 4391–4398.
56 S. J. An, J. Li, C. Daniel, D. Mohanty, S. Nagpure and D. L. Wood Iii, *Carbon*, 2016, **105**, 52–76.
57 Y. M. Zhao, Y. P. Cui, J. Shi, W. Liu, Z. C. Shi, S. G. Chen, X. Wang and H. L. Wang, *J. Mater. Chem. A*, 2017, **5**, 15243–15252.
58 X. Tang, G. Sui, Q. Cai, W. Zhong and X. Yang, *J. Mater. Chem. A*, 2016, **4**, 2082–2088.
59 L. Sheng, S. Liang, T. Wei, J. Chang, Z. Jiang, L. Zhang, Q. Zhou, J. Zhou, L. Jiang and Z. Fan, *Energy Storage Materials*, 2018, **12**, 94–102.
60 G. Carbonari, F. Maroni, M. Pasqualini, R. Tossici and F. Nobili, *Electrochim. Acta*, 2017, **247**, 392–399.
61 J. T. S. Irvine, D. C. Sinclair and A. R. West, *Adv. Mater.*, 1990, **2**, 132–138.
62 E. Peled and S. Menkin, *J. Electrochem. Soc.*, 2017, **164**, A1703–A1719.
63 S. Shi, Y. Qi, H. Li and L. G. Hector, *J. Phys. Chem. C*, 2013, **117**, 8579–8593.
64 J. Mizusaki, H. Tagawa, K. Saito, K. Uchida and M. Tezuka, *Solid State Ionics*, 1992, **53–56**, 791–797.
65 H. Li, G. Richter and J. Maier, *Adv. Mater.*, 2003, **15**, 736–739.
66 M. Sevilla and R. Mokaya, *Energy Environ. Sci.*, 2014, **7**, 1250–1280.
67 W. J. Cao and J. P. Zheng, *J. Power Sources*, 2012, **213**, 180–185.
68 R. Wang, J. Lang, P. Zhang, Z. Lin and X. Yan, *Adv. Funct. Mater.*, 2015, **25**, 2270–2278.
69 H. Wang, Y. Zhang, H. Ang, Y. Zhang, H. T. Tan, Y. Zhang, Y. Guo, J. B. Franklin, X. L. Wu, M. Srinivasan, H. J. Fan and Q. Yan, *Adv. Funct. Mater.*, 2016, **26**, 3082–3093.
70 C. Liu, S. Wang, C. Zhang, H. Fu, X. Nan, Y. Yang and G. Cao, *Energy Storage Materials*, 2016, **5**, 93–102.